Effects of the diameter of thermally generated nanopits on carrier dynamics in AlGaN/GaN heterostructures

Mohamed Bouzidi,[a,b,*] Wafa Malek,[b] Noureddine Chaaben,[b] Abdullah S. Alshammari,[a] Ziaul Raza Khan,[a] Mohamed Gandouzi,[a] Monsour Mohamed,[a] Ahmed Rebey,[c] Abdullah A. Alatawi,[d] Abdullah I. Alhassan,[d] Abdullah Alharbi,[d] Jean Paul Salvestrini,[e,f] and Mohammad Khaled Shakfa[g]

[a]University of Ha'il, College of Science, Department of Physics, Ha'il, Saudi Arabia
[b]Université de Monastir, Laboratoire de recherche sur les Hétéro-Epitaxies et Applications, Faculté des Sciences de Monastir, Monastir, Tunisia
[c]Qassim University, College of Science, Department of Physics, Buraidah, Saudi Arabia
[d]King Abdulaziz City for Science and Technology, Riyadh, Saudi Arabia
[e]International Research Lab Georgia Tech—CNRS, Georgia Tech Lorraine, Metz, France
[f]Georgia Institute of Technology, School of Electrical and Computer Engineering, Atlanta, Georgia, United States
[g]Philipps-Universität Marburg, Faculty of Physics and Materials Sciences Center, Marburg, Germany

Abstract The size and density of nanopits, generated at the surface of their top layer, strongly affect the electrical and optical properties of AlGaN-based structures. Therefore, the control of the layer quality evolution as a function of the nanopits size/density is a crucial issue to enhance the device performance. In this paper, the effects of the nanopits diameter observed at the surface of AlGaN on carrier dynamics are systematically investigated. The variation of nanopits diameter is achieved through thermal annealing of a set of AlGaN/GaN heterostructures at different temperatures. The samples are characterized using the scanning electron microscope (SEM), energy-dispersive x-ray, high-resolution x-ray diffraction, photoluminescence (PL), and time-resolved PL spectroscopies. SEM images have revealed an increase in the nanopits diameter with increasing annealing temperature. In addition, we observed a linear development in the yellow luminescence intensity, accompanied by a deterioration in the PL decay times due to an increase in the density of point-defect complexes that act as nonradiative recombination centers. We also performed temperature-dependent PL measurements to study the impact of the nanopits diameter on electron–phonon scattering processes. Both electron-acoustic- and electron-longitudinal optical phonon interactions enhance with increasing nanopits diameter. © 2022 Society of Photo-Optical Instrumentation Engineers (SPIE) [DOI: 10.1117/1.OE.61.10.105106]

1 Introduction

AlGaN ternary alloys have attracted increasing attention in the last decades due to their excellent physical properties, such as large and direct bandgap, high electron mobility, high thermal conductivity, high breakdown field, and great mechanical stability.[1–5] In addition, when varying the Al content, the bandgap of AlGaN varies from 3.4 eV for GaN to 6.2 eV for AlN, covering a broad spectral range.[5–8] This makes AlGaN and their based heterostructures very promising for the realization of a number of electronic and optoelectronic devices, such as high electron mobility transistors (HEMT),[9–11] metal–oxide semiconductor (MOS) HEMT,[12] MOS heterostructures

*Address all correspondence to M. Bouzidi, elbouzidimed16@yahoo.com

field-effect transistor,[13,14] ultra-violate (UV) light-emitting diodes (LEDs),[15–18] and solar-blind UV photodetectors.[19–21]

Yet, the performance of AlGaN-based devices has been limited by some challenging issues connected to the AlGaN layer quality,[4,8,22] e.g., the relatively low internal quantum efficiency, the poor p-type doping efficiency, and hardly achievable n- and p-type good ohmic contacts.[8,23] The primary factor responsible for the issues mentioned above is the presence of high dislocation and point-defect densities in the AlGaN epilayer due to heteroepitaxy on foreign substrates.[4,15] Isolated point defects and/or point defects coupled with dislocations create deep levels, act as scattering centers for light, and increase the nonradiative recombination rate.[4,24] Hence, reducing point defects in AlGaN layers is the key to improving the performance of AlGaN-based devices. For this purpose, various strategies and growth techniques have been suggested, such as the epitaxial lateral overgrowth,[15] the SiN treatment of sapphire substrate,[25] the deposition of low-temperature GaN or AlN buffer layer,[26] and the insertion of high-temperature GaN template layer between the buffer layer and the AlGaN active layer.[4] Despite the noticeable improvement in the layer quality using the aforementioned methods, the density of point defects in AlGaN is still higher than the level aimed to reach the full potential of AlGaN-based applications and devices. Post-growth treatments could help to improve (Al)GaN structure quality and hence the device performance. In this context, thermal annealing has been used to reduce the point defect density, to activate dopant atoms, and to achieve high-quality n- and p-type ohmic contacts.[27–29] Moreover, thermal annealing has been used to modify the surface properties of III-nitrides materials through thermal decomposition of the layer surface.[28,29] Consequently, nanostructures and nanopits with controllable size and density could be obtained. The size and density are strongly influenced by serval annealing parameters, such as the ambient gas (H_2, N_2, NH_3, or mixture), the geometry of the reactor (horizontal or vertical reactor), the polarity of the surface, the initial surface morphology, the annealing duration, and the annealing temperature.[28] Although, the structural features and the formation mechanism of these nanopits have been widely investigated, less attention has been paid to investigating the effects of nanopits diameter on the carrier dynamics in AlGaN. In this paper, a set of AlGaN/GaN heterostructures has been annealed at various temperatures to obtain AlGaN surfaces with nanopits at different diameters. The effects of the increasing diameter of nanopits on the structural and optical properties of AlGaN have been systematically analyzed. In particular, the yellow luminescence (YL) intensity, carrier decay times, and electron–phonon interaction evolutions as a function of the diameter of nanopits are discussed throughout the paper.

2 Experiments

The samples studied in the present work are a set of AlGaN/GaN heterostructures grown on SiN treated (0001) sapphire substrates by metal-organic vapor phase epitaxy and post-growth annealed at different temperatures. Ammonia (NH_3), trimethylaluminum, trimethylgallium, and silane (SiH_4) were used as N, Al, Ga, and Si sources, respectively. During the growth process, a mixture of N_2 and H_2 was used as the carrier gas. After cleaning the sapphire substrates, the growth started with a nitridation step for 10 min at 1080°C, under an ambient of $NH_3 + N_2 + H_2$. An *in-situ* thin Si/N mask was deposited on the sapphire substrate. Then, the temperature was decreased to 600°C for the deposition of a nominal 40-nm-thick GaN buffer layer. Afterward, a 0.7-μm thick-GaN template was deposited at 1080°C, followed by the growth of 0.4-μm thick AlGaN epilayer. The layer thicknesses of the GaN-template and AlGaN active layer were determined using *in-situ* reflectivity during the growth process.[30–32] More detail on the growth process can be found in Refs. 4, 29, 33, and 34.

After growth, the AlGaN/GaN/sapphire sample, i.e., wafer, was divided into five pieces labeled as A_0, A_1, A_2, A_3, and A_4. While sample A_0 was taken as a reference (as-grown sample), other samples A_1, A_2, A_3, and A_4, were annealed for 15 min under N_2 atmosphere at 1050°C, 1100°C, 1150°C, and 1200°C, respectively. The structural quality of the studied layers was assessed by high-resolution x-ray diffraction measurements using a Bruker D8 Discover system (45 kV, 40 mA) with a copper anode of *Ka* wavelength line of 1.5418 Å. Changes in the AlGaN surface morphology due to annealing treatment were *ex-situ* observed by scanning electron

microscope. Photoluminescence (PL) measurements were carried out using a 325-nm line of He-Cd laser as the excitation source. The PL emission was detected using a photomultiplier tube (Hamamatsu R-928) connected to a Spectra Pro 2500 spectrometer. For time-resolved PL (TRPL) measurements, a frequency-tripled mode-locked Ti:sapphire laser was used as an excitation source. The pump laser, emitting 100-fs pulses at a repetition rate of 80 MHz, was operated at a center wavelength of 290 nm. The PL signal was spectrally dispersed by an imaging spectrometer and temporally resolved using a streak camera.

3 Results and Discussion

Figure 1 shows scanning electron microscope (SEM) images of the as-grown sample (A_0) and other ones (A_1, A_2, A_3, and A_4) annealed at different temperatures. The surface morphology of the unannealed AlGaN layer shows randomly distributed hexagonal nanopits with an average diameter of 50 nm. These nanopits are commonly observed in III-nitride heterostructures and associated with misfit and threading dislocation terminus.[35,36] While threading dislocations are generated through the coalescence of adjacent grains during growth, misfit dislocations are
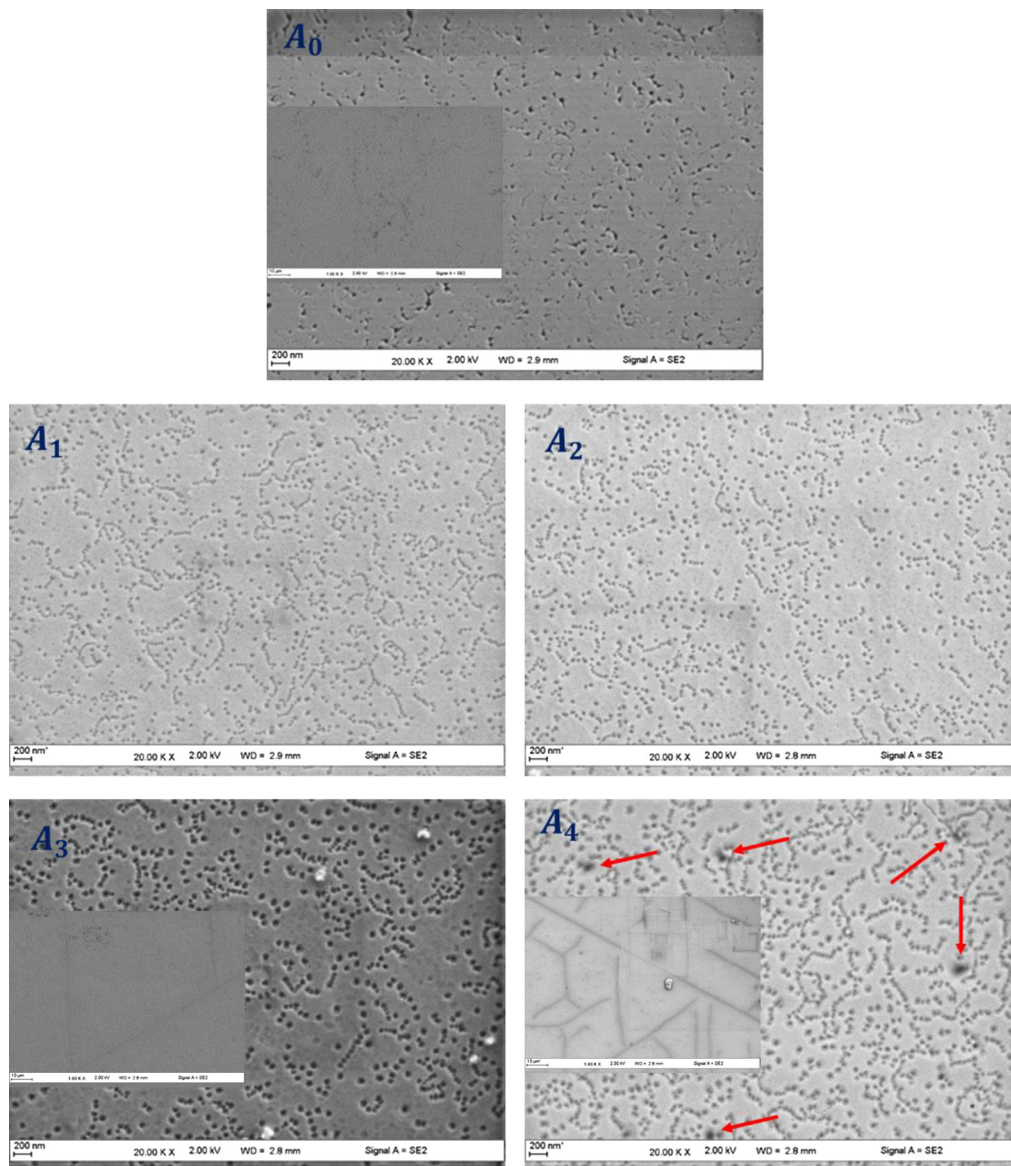

Fig. 1 SEM images of as-grown (A_0) and samples annealed at different temperatures (1050°C–1200°C: A_1 to A_4). The scale bar of inset images is 10 μm.

formed due to the internal stress caused by the lattice mismatch between the (Al)GaN layer and the substrate.[37] Misfit and threading dislocations can be entangled with each other during growth to form closed or open dislocation loops that prolong toward the top surface of the epitaxial layer. The density of nanopits for the as-grown layer is about 5.5×10^9 nanopits/cm^2. After samples' annealing, the diameter and the density of the nanopits changed. The nanopits density is about 6.2×10^9 nanopits/cm^2 and 5.8×10^9 nanopits/cm^2 in samples A_1 and A_2, respectively, and the nanopits diameter of about 40 nm is the same in both samples. The change in the nanopits density can be associated with the atoms' rearrangement and mater redistribution during the annealing process. When the annealing temperature is raised to 1150°C, the diameter of the nanopits increases from 40 nm to about 70 nm, but their density remains almost constant around 5.9×10^9 nanopits/cm^2. Simultaneously, cracks appear on the AlGaN top surface, as shown in the insert SEM image of sample A_3. The crack opening width is about 200 nm. For sample A_4, when the annealing temperature was further increased to 1200°C, the nanopits density increases to 6.3×10^9 nanopits/cm^2. Moreover, nanopits with a larger diameter of about 100 nm appear, as denoted by arrows in Fig. 1. Also, for sample A_4, the cracks density and width increase. Furthermore, we observed that the cracks prolong in different directions. The increase in the diameter of nanopits at relatively high annealing temperatures, 1150°C and 1200°C, reflects the start of the AlGaN thermal decomposition process. Indeed, thermal decomposition preferentially starts on dislocations sites generated on the top surface of the epitaxial layer[29,36,38] Our results agree well with the findings by Kuball et al.,[39] who have shown that AlGaN annealed in nitrogen ambient starts to decompose at annealing temperatures higher than 1150°C.

To determine the composition of the samples, we performed energy-dispersive x-ray measurements at different regions of each sample. The average atomic concentrations at the AlGaN surface of the as-grown and annealed samples are given in Table 1. The calculation of the Al/(Ga + Al) atomic ratio gives the same Al content of about $5.2 \pm 0.5\%$ in all samples. This result indicates that the annealing process has not affected the Al composition in the samples. Our observations agree well with that reported by Sarua et al.[40] In contrast, Kuball et al.[39] have observed that the annealing of $Al_{0.72}Ga_{0.28}N$ at a temperature higher than 1150°C results in an emergence of two $Al_xGa_{1-x}N$ phases with different Al compositions. The difference between our result and that of Kuball's group could be attributed to the high Al composition in their as-grown sample.

Furthermore, as given in Table 1, thermal annealing at a temperature higher than 1100°C resultes in an obvious increase in the oxygen (O) concentration at the AlGaN surface. Similar behavior has been observed by Hagedorn et al.[41] and Chen et al.[42] after high-temperature annealing of AlGaN layers. The increase of the O concentration, observed in our samples A_3 and A_4, could be attributed to the diffusion of O impurity (during the thermal treatment) from the sapphire interface toward the AlGaN top surface through the dislocation lines.

HR-XRD measurements were carried out to investigate the effect of annealing on the structural properties of the samples. Figure 2 shows the (00.4) (ω–2θ) scans of the studied AlGaN/GaN heterostructures, in which two peaks are obviously observed. While the low-angle peak corresponds to the GaN underlayer, the high-angle one is associated with the AlGaN epilayer. The peak shift on the ω–2θ scan is attributed to Al incorporation and the variation of strain in the

Table 1 The relative atomic concentration at the AlGaN surface and the lattice constants of the studied samples determined by EDX measurements.

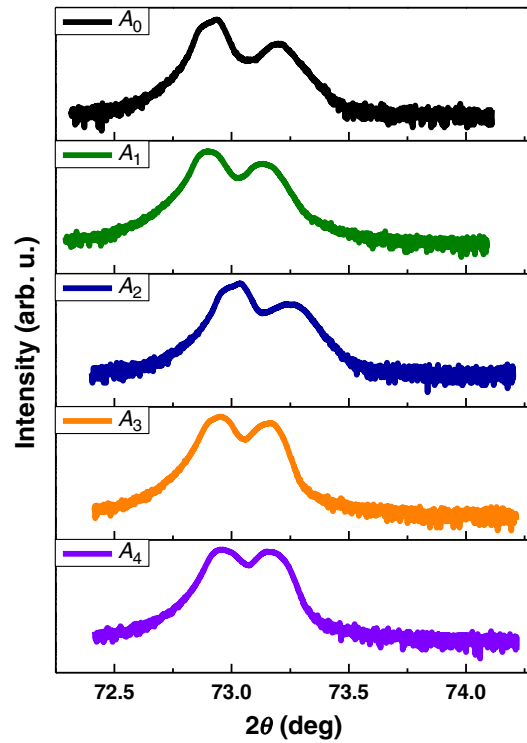| Sample	Annealing temperature (°C)	Ga (%)	Al (%)	N (%)	O (%)	a (Å)	c (Å)
A_0	—	59.5	3.3	23.6	13.6	3.1870	3.1740
A_1	1050	58.6	3.4	27.1	10.9	3.1930	3.1713
A_2	1100	51.5	2.8	36.9	8.8	3.1936	3.1711
A_3	1150	62.5	3.5	16.8	17.2	3.1871	3.1733
A_4	1200	54.6	3.1	20.0	22.3	3.1858	3.1746

Fig. 2 HR-XRD spectra in the ω–2θ scan mode around (00.4) symmetric reflection, recorded for as-grown sample (A_0) and annealed samples (A_1 to A_4).

heterostructures. Since the Al composition is almost the same for all samples, the peak shift observed in Fig. 2 is only ascribed to the strain variation. By taking the GaN peak as a reference, the Bragg angle of AlGaN (θ_{AlGaN}) is accurately obtained as

$$\theta_{AlGaN} = \theta_{GaN} + \Delta\theta, \tag{1a}$$

where $\Delta\theta$ is the angle difference between the AlGaN and GaN diffraction peaks. The out-of-plane lattice constant (c) of AlGaN is calculated using the Bragg angle of the AlGaN (00.4) plane and the Bragg equation:

$$2d_{hkl} \sin\theta = n\lambda, \tag{1b}$$

where, n is the order of diffraction and $\lambda = 1.5418$ Å is the x-ray wavelength. d_{hkl} is the inter-reticular distance given as

$$d_{hkl} = \frac{1}{\sqrt{\frac{4}{3a^2}(h^2 + k^2 + hk) + \frac{l^2}{c^2}}}. \tag{1c}$$

Likewise, using the Bragg angle of the AlGaN (-10.5) plane, Bragg equation, and the lattice constant c, the in-plane lattice constant (a) is determined. The lattice parameter values obtained for the differents samples are summarized in Table 1. Subsequently, the in-plane strain (ε_{xx}) and the out-of-plane strain (ε_{zz}) in our AlGaN layers are estimated as

$$\varepsilon_{xx} = \frac{a - a_0}{a_0}, \tag{2}$$

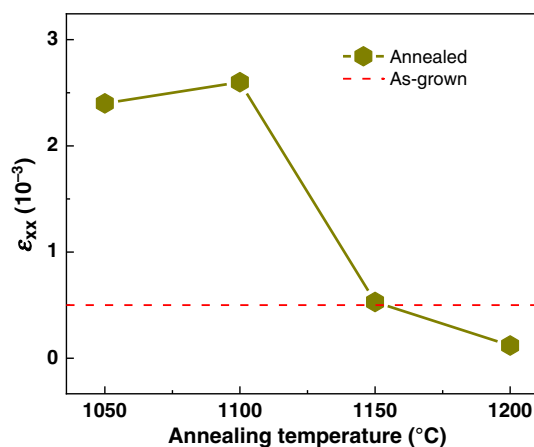$$\varepsilon_{zz} = \frac{c - c_0}{c_0}, \tag{3}$$

Fig. 3 In-plane strain evolution as a function of the annealing temperature.

where a_0 and c_0 are the strain-free AlGaN lattice constants, which are determined using linear interpolation between the literature values for unstrained GaN ($a_0^{GaN} = 3.1893$ Å; $c_0^{GaN} = 5.1851$ Å) and unstrained AlN ($a_0^{AlN} = 3.1130$ Å; $c_0^{AlN} = 4.9816$ Å).[7] The obtained in-plane strain in our samples is shown in Fig. 3 as a function of the annealing temperature. The positive value of ε_{xx} indicates the tensile nature of the strain, in agreement with previous studies for AlGaN deposited on GaN/sapphire.[4,7] The tensil-strain value for the as-grown sample is about 5×10^{-4}. After thermal treatment, the tensil-strain value first increases with increasing annealing temperature to reach a maximum of 2.6×10^{-3} at 1100°C. Above this temperature, the in-plane tensil-strain shows a significant decrease; its value drops to 0.53×10^{-3} and 0.12×10^{-3} when annealing at 1150°C and 1200°C, respectively. Such a behavior of the in-plane tensil-strain is typically associated with a relaxation process. The increase in the tensil-strain level as a function of the annealing temperature mainly results from an additional tensile strain generated during the thermal treatment due to the mismatch in thermal expansion coefficients between the substrate and the (Al)GaN layer.[28,43] The tensil-strain relaxation process after high-temperature annealing has been previously observed, and different mechanisms have been reported to explain this relaxation. Itokazu et al.[44] have stated that the release of strain energy accumulated in the crystal is attributed to the restoration of the crystallinity during the high-temperature annealing. Moreover, Sarua et al.[40] have observed a change in stress from tensile to compressive in AlGaN/GaN/sapphire heterostructures after thermal annealing above 800°C in air ambient; this compressive-strain is attributed to the O impurity incorporation into the AlGaN layer during annealing. Furthermore, Chen et al.[42] have reported that long-duration high-temperature annealing of AlGaN/GaN/sapphire heterostructure induced a lattice relaxation in the AlGaN layer due to the O impurity incorporation.

Gruber et al.[45] have found that the strain relaxation process was associated with vacancies created at the film surface. Based on the above-mentioned observations and the results obtained from SEM and EDX investigations, we conclude that two majors effects are responsible for the tensil-strain relaxation observed in samples A_3 and A_4: (i) the O incorporation induced compressive strain, which partially compensates the tensile strain already existed in the as-grown AlGaN layer, and (ii) the tensil-strain relaxation associated with the defect formation (such as vacancies and dislocations) during high-temperature annealing. It is worth noting that the tensile-strain relaxation in AlGaN/GaN/Sapphire heterostructures is frequently accompanied with cracks on the AlGaN top layer.[33,40,46] This is in agreement with our observations for samples A_3 and A_4 from SEM images shown in Fig. 1.

To examine the effects of the nanopits diameter on the optical properties of the samples, room-temperature PL measurements were carried out. The PL spectra of the samples are shown in Fig. 4; they are normalized with respect to the near-band-edge (NBE) peak emission of AlGaN at an energy of about 3.52 eV. The emission peaks at 3.41 and 2.33 eV are related to the NBE of GaN and to the YL peak, respectively.
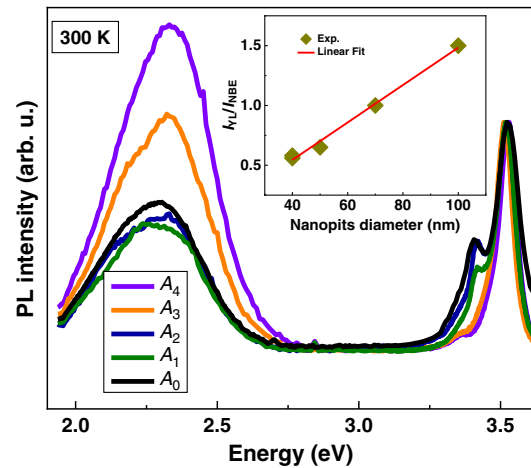
Fig. 4 Room temperature PL spectra of the samples, normalized to the NBE of the AlGaN layer. The inset shows the evolution of I_{YL}/I_{NBE} with the nanopits diameter.

The YL peak position shows a blue shift of 130 meV compared to the commonly observed YL energy postion of GaN at 2.2 eV.[22,47] This is in agreement with findings reported by Goyal et al.[22] Yet, this blue shift is proportional to the Al composition in AlGaN. A blue shift of the YL peak position of about 90 nm (400 meV) and 109 nm (500 meV) is observed for AlGaN layers with Al composition of about 26% and 30%, respectively.[22] Thus, the YL observed in the present work at 2.33 eV is attributed to the AlGaN layer. For the as-grown sample, the I_{YL}/I_{NBE} is about 0.65. After samples' annealing, this ratio decreases to be about 0.56 for samples A1 and A2. In contrast, the I_{YL}/I_{NBE} ratio increases and reaches a value of 1.5 when the annealing temperature was raised up to 1200°C. The mechanism of YL in (Al)GaN is typically associated with the radiative transition from shallow donor energy states to deep acceptor ones.[22,47] The macroscopic nature of this acceptor level has been the subject of several scientific works.[22,48] Dislocations, isolated points defects and/or point defect-related complexes have been suggested to be the origin of this deep acceptor level responsible for the YL emission in (Al)GaN. Macht et al.[49] have reported that the YL is more related to point defects rather than dislocations. Moreover, a number of theoretical studies supported with experimental observations have concluded that gallium vacancy (V_{Ga}) and/or gallium vacancy-related complexes, such as V_{Ga}-O_N, are the most probable defect type responsible for the YL in (Al)GaN.[22,47]

By combining the results of the SEM and PL measurements presented in this work, one can obviously conclude a correlation between the YL intensity and the nanopits diameter. The variation of the intensity ratio of the YL to the AlGaN NBE (I_{YL}/I_{NBE}) as a function of nanopits diameter is plotted in the inset of Fig. 4. Interestingly, the I_{YL}/I_{NBE} shows a linear increase with the increase of the nanopits diameter. The aforementioned increase of the YL intensity could be associated with the increase of dislocations and point defects densities in AlGaN layers. Indeed, as discussed from SEM results, the nanopits are associated with dislocation terminus, and their locations are characterized by high density of vacancies. Furthermore, owing to its small formation energy, a high density of V_{Ga} is expected around the nanopits sites. When the nanopits diameter is increased, the density of V_{Ga} increases, leading to an enhacement of the YL intensity.

TRPL measurements were carried out at room temperature. The normalized PL transients, measured at an average laser power of 0.3 mW, are shown in Fig. 5. The PL transients tend to be relatively longer with increasing annealing temperature up to 1100°C. Beyond this temperature, a shortening in the PL transition is observed. As shown by the solid lines in Fig. 5, the PL transients can be well fitted using a bi-exponential function:

$$I(t) = A_f \exp\left(-\frac{t}{\tau_f}\right) + A_s \exp\left(-\frac{t}{\tau_s}\right), \tag{4}$$

where $I(t)$ refers to the PL intensity at time t. $A_f(A_s)$ and $\tau_f(\tau_s)$ correspond to the initial intensity and the decay time, respectively, of the fast (slow) PL decay component.
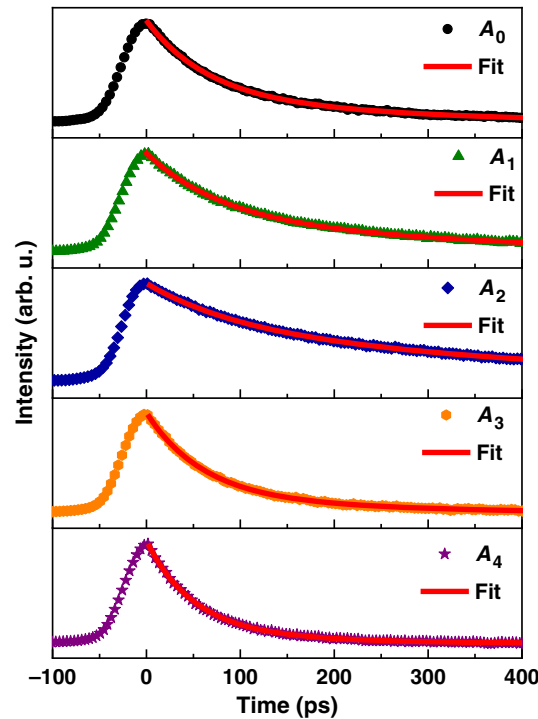
Fig. 5 Room temperature TRPL spectra of the as-grown sample (A_0) and annealed samples (A_1 to A_4). Symbols represent the experiment data while the solid lines are the least square fitting using Eq. (1).

For the as-grown sample, τ_f and τ_s are 64 and 260 ps, respectively, whereas A_s/A_f is about 0.41. Obviously, τ_f, τ_s, and A_s/A_f increase with the annealing temperature (nanopits diameter) to reach a maximum value of about 94 and 440 ps, and 1.5, respectively, when the annealing temperature is increased up to 1100°C (sample A_2). Yet, when the annealing temperature is further increased, a drop in both τ_f and τ_s and the A_s/A_f intensity ratio is observed.

According to Refs. 4, 24, 50, and 51, the slow and fast components are connected to the presence of two dominant recombination pathways that contribute to the decay curve. Moreover, an increased A_s/A_f ratio reflects a reduction in the contribution of nonradiative relaxation pathways. Therefore, the increase of the A_s/A_f intensity ratio, observed for samples A_1 and A_2 compared to sample A_0, clearly indicates a decrease in the density of nonradiative recombination centers in the AlGaN layer after the annealing at 1050°C and 1100°C. Likewise, the drop in the A_s/A_f ratio observed for samples A_3 and A_4 reflects an increase in the density of nonradiative recombination centers when the annealing temperature is increased beyond 1100°C. After Refs. 52 and 53, the origin of the predominant nonradiative recombination centers in (Al)GaN at room temperature are (i) point defect complexes, (ii) III-element vacancies, such as Al vacancy with nitrogen-vacancy (V_{Al}-V_N), (iii) Al vacancy with oxygen impurity in nitrogen site (V_{Al}-O_N), and (iv) Ga vacancy with oxygen impurity in nitrogen site (V_{Ga}-O_N).

From Figs. 4 and 5, it can be seen that both the YL emission and the carrier decays show an inverse trend when the annealing temperature (nanopits diameter) is increased; when the enhancement in the YL intensity is accompanied by a decrease in the luminescence decay times, the drop of the YL intensity corresponds to an increase in the luminescence decay times. This observation strongly suggests that the type of defects responsible for the rise of the YL emission is also responsible for the shortening of the PL decay. Figures 6(a), 6(b), and 6(c) show the variation of the decay times and the intensity ratio of the slow PL component to the fast one (A_s/A_f) as a function of the nanopits diameter. One can see that both τ_f and τ_s decrease gradually with increasing nanopits diameter. However, the fast process is more affected by the nanopits diameter, as illustrated by its more rapid slope compared to the slow process. On the other hand, while the A_s/A_f ratio is strongly affected by nanopits diameter until 50 nm, a relatively less
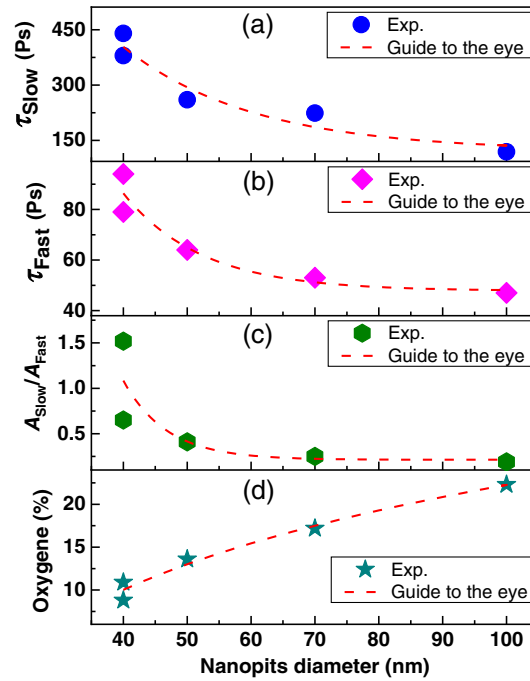
Fig. 6 (a) Slow decay time; (b) fast decay time; (c) A_s/A_f intensity ratio; and (d) oxygen concentration, against nanopits diameter.

pronounced effect is observed when the nanopits diameter becomes higher than 50 nm. Figure 6(d) shows the variation of the O concentration in the samples as a function of the nanopits diameter. Obviously, the O concentration increases when the nanopits diameter is increased. The aforementioned behavior has been strongly expected. In fact, the sapphire substrate is the primary source of oxygen impurity in AlGaN/GaN/Al$_2$O$_3$ heterostructures. When the nanopits diameter is increased, the concentration of diffused O impurity (through the dislocation lines) from the sapphire interface toward the AlGaN top surface increases. Hence, we conclude that the shortening of the PL transient as a function of nanopits diameter can be attributed to a rise in the density of complexes formed by *Ga* vacancy and oxygen impurity, such as Ga vacancy with oxygen impurity in nitrogen-vacancy (V_{Ga}-O_N).

To investigate the impact of nanopits diameter on the electron–phonon interactions, temperature-dependent PL measurements were performed for samples A_0, A_2, and A_4, in the temperature range 10 to 300 K. The spectra obtained for samples A_0 and A_4 are shown in Fig. 7. When the temperature is increased, the emission peak of AlGaN becomes broadened and shifts toward the lower energy side. This behavior is attributed to the temperature-induced shrinkage of the bandgap energy and to an enhancement of the electron–phonon scattering.[54] Figure 8 shows the variation of the linewidth of AlGaN-emission-peak as a function of temperature for samples A_0, A_2, and A_4. The linewidth values of the AlGaN emission peak are obtained by a Gaussian fit of the PL spectra at each temperature, as shown in the insets of Fig. 7. Based on Refs. 54 and 55, the thermal broadening of the linewidth of the bandgap emission can be described by the following expression:

$$\Gamma(T) = \Gamma_0 + \alpha_{ac}T + \Gamma_{imp}\exp\left(\frac{-\langle E_b\rangle}{kT}\right) + \Gamma_{LO}\frac{1}{\exp\left(\frac{\theta_{LO}}{kT}\right) - 1}, \qquad (5)$$

where, Γ_0 is the inhomogeneous broadening that is independent of temperature and ascribed to collision with intrinsic defects such as dislocations and interface roughness. The second term ($\alpha_{ac}T$) is the linewidth due to the electron-acoustic phonon scattering, where α_{ac} represents the electron-acoustic phonon coupling strength. The third term represents the thermal broadening of the emission line due to electron-scattering with thermal ionized impurities. Γ_{imp} is the linewidth
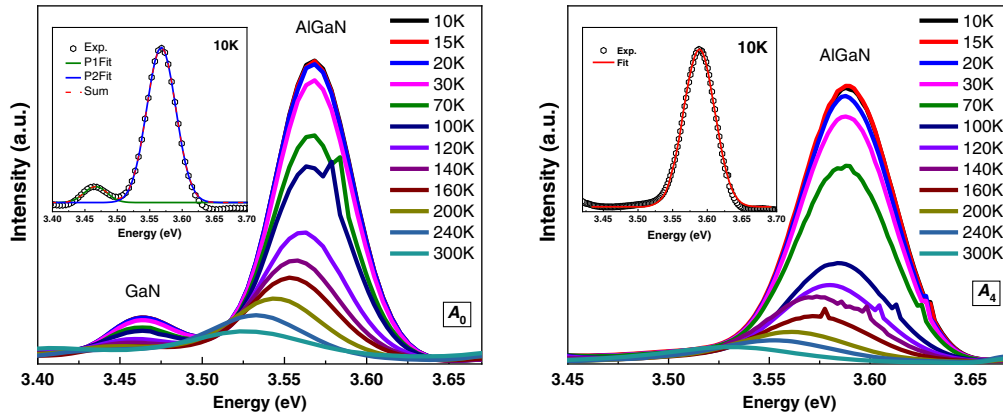
Fig. 7 Temperature dependence photoluminescence spectra for samples A_1 and A_4. The insets show an example of the Gaussian fits of experimental data. Some of the spectra show a small sharp peak due to an uncontrollable mechanical movement/jump of the grating of the monochromator.
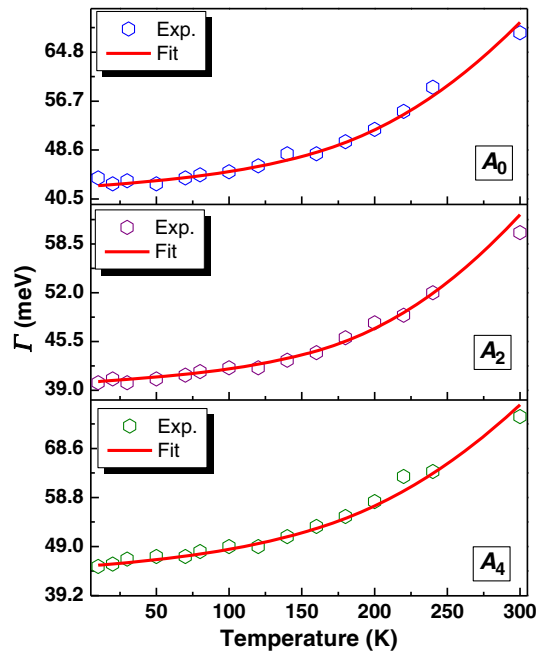

Fig. 8 Temperature dependence of the AlGaN emission linewidth measured for samples A_0, A_2, and A_4. Symbols are the experimental data, and the red lines are the least-square fits using Eq. (5).

due to the fully ionized impurity scattering, which is proportional to the impurity concentration in the layers. $\langle E_b \rangle = 29$ meV is the average value over all possible donor-impurity binding energies,[54,55] and k is the Boltzmann constant. The last term in Eq. (5) is the linewidth broadening due to electron-longitudinal optical (LO) phonon scattering, where Γ_{LO} is the strength of this interaction. $\theta_{LO} = 93$ meV is the LO phonon energy in $Al_{0.05}Ga_{0.95}N$, which is obtained by linear interpolation between the literature values for GaN (92 meV)[54] and AlN (110 meV).[56]

The experimental data of the PL emission linewidth, for samples A_0, A_1, and A_4, are least-squares fitted using Eq. (5) as shown by the red lines in Fig. 8. Fitting parameters are summarized in Table 2. Both Γ_0 and Γ_{imp} increase with increasing nanopits diameter, i.e., the larger the nanopits diameter, the higher the defect density (e.g., point defect, dislocations, and impurity) in the sample. Furthermore, as observed from Table 2, α_{ac} and Γ_{LO} increase from 15 to 27 μeV/K, and from 520 to 618 meV, respectively, when the nanopits diameter is increased from 40 to 100 nm.

Table 2 Fitting parameters that describe the temperature dependence of the PL emission line-width, obtained by least-squares fitting of experimental data using Eq. (5).

Sample	Nanopits diameter (nm)	Γ_0 (meV)	α_{ac} (μeV/K)	Γ_{imp} (meV)	Γ_{LO} (meV)
A_2	40	40 ± 0.2	15 ± 1	10 ± 1	520 ± 10
A_0	50	43 ± 0.2	20 ± 1	15 ± 1	580 ± 10
A_4	100	45 ± 0.2	27 ± 1	21 ± 1	618 ± 10

This indicates that increasing nanopits diameter leads to an enhancement in electron-acoustic- and electron-longitudinal optical phonon scattering processes. The electron-acoustic phonon interaction is manifested via the deformation potential mechanism and piezoelectric interaction. In contrast, the exciton–LO phonon interaction occurs via the deformation potential scattering and the Fröhlich interaction.[54] Evgenii et al.[57] reported that the built-in electric field in AlN/GaN/AlN heterostructures enhances the electron–phonon interaction via the deformation potential and the piezoelectric potential. In our samples, when the nanopits diameter is increased, the built-in electric field is expected to rise due to increasing defect density.[4,37]

The enhancement in the electron–phonon coupling strength can also be attributed to the variation of electron–phonon scattering rates, resulting from the change of the strain level in the AlGaN layer when the diameter of nanopits is increased. Indeed, Tang et al.[58] reported that electron–phonon scattering rates decrease with tensile strain. In our case, when the diameter of nanopits is increased from 40 to 100 nm, the tensile strain decreases from 2.4×10^{-3} to 0.12×10^{-3}, leading to an enhancement of electron–phonons scattering.

Ultimately, it is worth pointing out that the values of α_{ac} and Γ_{LO} obtained in this work are comprised between those reported for GaN ($\alpha_{ac} \approx 5 - 10 \ \mu$eV/K; $\Gamma_{LO} \approx 255$ meV)[54] and AlN ($\alpha_{ac} \approx 57 \ \mu$eV/K; $\Gamma_{LO} \approx 1245$ meV).[56] However, our values differ slightly from those obtained by Murotani et al.[59] for $Al_{0.057}Ga_{0.943}N$/GaN heterostructures: ($\alpha_{ac} \approx 18 \ \mu$eV/K; $\Gamma_{LO} \approx 680$ meV). The small difference between our and previously reported values can be explained by two primary reasons. The first one is connected to the difference in the qualities between our and their samples in terms of, e.g., strain level, defect density, morphology, and internal electric field, which influence the electron–phonons scattering processes. The second reason is due to the fact that Murotani et al. ingnored the scattering with thermal ionized impurity when analyzing the thermal broadening of linewidth, which causes an overestimation, especially in the value of Γ_{LO}.

4 Conclusion

Thermal annealing has been utilized to create nanopits at the top surface of AlGaN/GaN heterostructures. The influence of the annealing temperature on the nanopits diameter and structural properties of AlGaN/GaN heterostructures has been investigated. SEM images show that annealing at temperatures higher than 1100°C leads to an increase in the diameter of the nanopits, accompanied by cracks. HRXRD measurements reveal that annealing at temperatures below 1100°C induces additional tensile strain, whereas annealing at a temperature above 1100°C results in tesile strain relaxation. Furthermore, the effects of the diameter of nanopits on the carrier dynamics in have been investigated using PL and TRPL spectroscopies. Room-temperature PL measurements have showed that the YL intensity increases linearly with the diameter of nanopits. TRPL results exhibit the contribution of two processes to the PL decay, i.e., fast and slow components, which both decrease when the diameter of the nanopits is increased. This decrease is due to an increase in the density of point-defect complexes that act as nonradiative recombination centers. Our investigations have also shown that the increase of nanopits diameter enhances the electron-acoustic phonon and the electron-longitudinal optical phonon interactions. This enhancement is associated with the rise of the defect density and the decrease in the tensile strain in the AlGaN layer when the diameter of nanopits is increased.

Acknowledgments

References

1. M. Wośko et al., "MOVPE growth conditions optimization for AlGaN/GaN/Si heterostructures with SiN and LT-AlN interlayers designed for HEMT applications," *J. Mater. Sci. Mater. Electron.* **30**, 4111–4116 (2019).
2. Y. Tian et al., "Reduction of hexagonal defects in N-polar AlGaN epitaxial layers grown with reformed pulsed-flow technology," *Mater. Sci. Semicond. Process.* **138**, 106312 (2022).
3. C. Liu et al., "Influence of Al pre-deposition time on AlGaN/GaN heterostructures grown on sapphire substrate by metal organic chemical vapor deposition," *J. Mater. Sci. Mater. Electron.* **31**, 14737–14745 (2020).
4. M. Bouzidi et al., "Correlation of structural and optical properties of AlGaN films grown on SiN-treated sapphire by MOVPE," *Mater. Sci. Eng. B Solid-State Mater. Adv. Technol.* **263**, 114866 (2021).
5. L. Lu et al., "Impact of composite last quantum barrier on the performance of AlGaN-based deep ultraviolet light-emitting diode," *J. Mater. Sci. Mater. Electron.* **32**, 18138–18144 (2021).
6. W. Y. Han et al., "High performance back-illuminated MIS structure AlGaN solar-blind ultraviolet photodiodes," *J. Mater. Sci. Mater. Electron.* **29**, 9077–9082 (2018).
7. T. T. Luong et al., "Phase separation-suppressed and strain-modulated improvement of crystalline quality of AlGaN epitaxial layer grown by MOCVD," *Microelectron. Reliab.* **83**, 286–292 (2018).
8. Y. Chen et al., "Review on the progress of AlGaN-based ultraviolet light-emitting diodes," *Fundam. Res.* **1**, 717–734 (2021).
9. M. Gassoumi, "Characterization of deep levels in AlGaN | GaN HEMT by FT-DLTS and current DLTS," *Semiconductors* **54**, 1296–1303 (2020).
10. A. Buffer et al., "MBE AlGaN/GaN HEMT heterostructures," *Semiconductors* **52** (2018) 2107–2110.
11. E. V Erofeev et al., "Low-temperature Ta/Al-based ohmic contacts to AlGaN/GaN heteroepitaxial structures on silicon wafers," *Semiconductors* **53**, 237–240 (2019).
12. Y. Li et al., "Growth of high-quality AlGaN epitaxial films on Si substrates," *Mater. Lett.* **207**, 133–136 (2017).
13. L. He et al., "Correlating device behaviors with semiconductor lattice damage at MOS interface by comparing plasma-etching and regrown recessed-gate Al_2O_3/GaN MOS-FETs," *Appl. Surf. Sci.* **546**, 148710 (2021).
14. Q. Meng et al., "Characterization of the electrical properties of a double heterostructure GaN/AlGaN epitaxial layer with an AlGaN interlayer," *J. Electron. Mater.* **50**, 2521–2529 (2021).
15. A. Nasir et al., "Effects of indium surfactant and MgN intermediate layers on surface morphology and crystalline quality of nonpolar a-plane AlGaN epi-layers," *Optik (Stuttgart)* **192**, 162978 (2019).
16. R. Kumar et al., "Recent advances and challenges in AlGaN-based ultra-violet light emitting diode technologies," *Mater. Res. Bull.* **140**, 111258 (2021).
17. N. U. Islam et al., "Remarkable efficiency improvement in AlGaN-based ultraviolet light-emitting diodes using graded last quantum barrier," *Optik (Stuttgart)* **248**, 168212 (2021).
18. T. Jamil et al., "High radiative recombination rate of AlGaN-based deep ultraviolet light – emitting diodes with AlInGaN/AlInN/AlInGaN tunnel electron blocking layer," *J. Electron. Mater.* **50**, 5612–5617 (2021).
19. Y. Chen et al., "Dual-band solar-blind UV photodetectors based on AlGaN/AlN superlattices," *Mater. Lett.* **291**, 129583 (2021).
20. Y. Chen et al., "Epitaxial growth of polarization-graded AlGaN-based solar-blind ultraviolet photodetectors on pre-grown AlN templates," *Mater. Lett.* **281**, 128638 (2020).

21. Z. Zhang et al., "Separate absorption and multiplication AlGaN solar-blind avalanche photo-diodes with high-low-doped and heterostructured charge layer," *J. Electron. Mater.* **49**, 2343–2348 (2020).

22. A. Goyal et al., "Non destructive evaluation of AlGaN/GaN HEMT structure by cathodo-luminescence spectroscopy," *J. Lumin.* **232**, 117834 (2021).

23. M. Usman et al., "Optik designing anti-trapezoidal electron blocking layer for the amelio-ration of AlGaN-based deep ultraviolet light-emitting diodes internal quantum efficiency," *Optik (Stuttgart)* **232**, 166528 (2021).

24. M. Bouzidi et al., "Time-resolved photoluminescence and photoreflectance spectroscopy of GaN layers grown on SiN-treated sapphire substrate: optical properties evolution at different growth stages," *Opt. Mater. (Amst.)* **73**, 252–259 (2017).

25. K. Forghani et al., "*In-situ* deposited SiNx nanomask for crystal quality improvement in AlGaN," *Phys. Status Solidi C* **8**(7–8), 2063–2065 (2011).

26. M. Jayasakthi et al., "Influence of AlN thickness on AlGaN epilayer grown by MOCVD," *Superlattices Microstruct.* **98**, 515–521 (2016).

27. N. I. S. Nakamura, T. Mukai, and M. Senoh, "Thermal annealing effects on p-type Mg-doped GaN films," *Jpn. J. Appl. Phys.* **31**, L139–L142 (1992).

28. W. Malek et al., "Optical characterization by photoreflectance of GaN after its partial thermal decomposition," *Optik (Stuttgart)* **248**, 168070 (2021).

29. H. Bouazizi et al., "Observation of the early stages of GaN thermal decomposition at 1200°C under N_2," *Mater. Sci. Eng. B Solid-State Mater. Adv. Technol.* **227**, 16–21 (2018).

30. W. Malek et al., "Optik *in situ* spectral reflectance analysis of the early stages of GaN thermal decomposition," *Optik (Stuttgart)* **265**, 169491 (2022).

31. N. Chaaben et al., "High resolution X-ray diffraction of GaN grown on Si (1 1 1) by MOVPE," *Appl. Surf. Sci.* **253**, 241–245 (2006).

32. N. Chaaben et al., "Materials science in semiconductor processing study of Al diffusion in GaN during metal organic vapor phase epitaxy of AlGaN/GaN and AlN/GaN structures," *Mater. Sci. Semicond. Process.* **42**, 359–363 (2016).

33. I. Halidou et al., "Effect of GaN template thickness and morphology on $Al_xGa_{1-x}N$ ($0 < x < 0.2$) growth by MOVPE," *Appl. Surf. Sci.* **280**, 660–665 (2013).

34. M. Bouzidi et al., "Superlattices and microstructures photoreflectance study of GaN grown on SiN treated sapphire substrate by MOVPE," *Superlattices Microstruct.* **84**, 13–23 (2015).

35. K. Jiang et al, "Suppressing the luminescence of V_{cation}-related point-defect in AlGaN grown by MOCVD on HVPE-AlN," *Appl. Surf. Sci.* **520**, 1–9 (2020).

36. Y. Zhang et al., "Influence of dislocations on the thermal decomposition of GaN," *Mater. Lett.* **249**, 25–28 (2019).

37. A. Sangghaleh et al., "Near-interface charged dislocations in AlGaN/GaN bilayer hetero-structures near-interface charged dislocations in AlGaN/GaN bilayer heterostructures," *Appl. Phys. Lett.* **105**, 102102 (2014).

38. H. Bouazizi et al., "Study of the partial decomposition of GaN layers grown by MOVPE with different coalescence degree," *J. Cryst. Growth* **434**, 72–76 (2016).

39. M. Kuball et al., "Degradation of AlGaN during high-temperature annealing monitored by ultraviolet Raman scattering," *Appl. Phys. Lett.* **74**, 549–551 (1999).

40. A. Sarua et al., "High temperature annealing of AlGaN: Stress and composition changes," *Phys. Status Solidi C Conf.* **571**, 568–571 (2002).

41. S. Hagedorn et al., "High-temperature annealing of AlGaN," *Phys. Status Solidi Appl. Mater. Sci.* **217**, 2000473 (2020).

42. D.J. Chen et al., "The effect of long-duration higherature annealing in an air ambient on the properties of AlGaNGaN heterostructures," *J. Appl. Phys.* **103**, 1–4 (2008).

43. S. Einfeldt et al., "Strain relaxation in AlGaN under tensile plane stress," *J. Appl. Phys.* **88**, 7029–7036 (2000).

44. Y. Itokazu et al., "Influence of the nucleation conditions on the quality of AlN layers with higherature annealing and regrowth processes," *Jpn. J. Appl. Phys.* **58**, SC1056 (2019).

45. W. Gruber et al., "Strain relaxation and vacancy creation in thin platinum films," *Phys. Rev. Lett.* **107**, 1–5 (2011).

46. S. Rajasingam et al., "High-temperature annealing of AlGaN: stress, structural, and compositional changes," *J. Appl. Phys.* **94**, 6366–6371 (2003).
47. P. Kamyczek et al., "A deep acceptor defect responsible for the yellow luminescence in GaN and AlGaN," *J. Appl. Phys.* **111**, 113105 (2012).
48. M. A. Reshchikov et al., "Two yellow luminescence bands in undoped GaN," *Sci. Rep.* **8**, 8091 (2018).
49. L. Macht et al., "Statistical photoluminescence of dislocations and associated defects in heteroepitaxial GaN grown by metal organic chemical vapor deposition," *Phys. Rev. B – Condens. Matter Mater. Phys.* **71**, 2–5 (2005).
50. Ü. Özgür et al., "Long carrier lifetimes in GaN epitaxial layers grown using TiN porous network templates," *Appl. Phys. Lett.* **86**, 1–3 (2005).
51. J. Xie et al., "Low dislocation densities and long carrier lifetimes in GaN thin films grown on a Si Nx nanonetwork," *Appl. Phys. Lett.* **90**, 2005–2008 (2007).
52. S. Ichikawa, M. Funato, and Y. Kawakami, "Dominant nonradiative recombination paths and their activation processes in Al$_x$Ga$_{1-x}$N-related materials," *Phys. Rev. Appl.* **10**, 1 (2018).
53. S. F. Chichibu et al., "The origins and properties of intrinsic nonradiative recombination centers in wide bandgap GaN and AlGaN," *J. Appl. Phys.* **123**, 161413 (2018).
54. M. Bouzidi et al., "Effects of thermal ionized-impurities and mosaicity on the excitonic properties of GaN grown by MOVPE," *Optik (Stuttgart)* **142**, 144–152 (2017).
55. O. Aoudé et al., "Continuous-wave and ultrafast coherent reflectivity studies of excitons in bulk GaN," *Phys. Rev. B* **77**, 045206 (2008).
56. K. B. Nam et al., "Optical properties of AlN and GaN in elevated temperatures," *Appl. Phus. Lett.* **85**, 3489 (2004).
57. E. P. Pokatilov et al., "Confined electron-confined phonon scattering rates in wurtzite AlN/GaN/AlN heterostructures," *J. Appl. Phys.* **95**, 5626 (2014).
58. D.-S. Tang et al. "Thermal transport properties of GaN with biaxial strain and electron-phonon coupling," *J. Appl. Phys.* **127**, 035102 (2020).
59. H. Murotani et al., "Temperature dependence of localized exciton transitions in AlGaN ternary alloy epitaxial layers," *J. Appl. Phys.* **104**, 053514 (2008).

Biographies of the authors are not available.